Science
AAAS

Transient Simulation of Last Deglaciation with a New Mechanism for Bølling-Allerød Warming
Z. Liu, *et al.*
Science **325**, 310 (2009);
DOI: 10.1126/science.1171041

14. M. E. Raymo, W. F. Ruddiman, J. Backman, B. M. Clement, D. G. Martinson, *Paleoceanography* **4**, 413 (1989).
15. P. A. Martin *et al.*, *Earth Planet. Sci. Lett.* **198**, 193 (2002).
16. H. Elderfield, J. Yu, P. Anand, T. Kiefer, B. Nyland, *Earth Planet. Sci. Lett.* **250**, 633 (2006).
17. J. Yu, H. Elderfield, *Earth Planet. Sci. Lett.* **276**, 129 (2008).
18. N. J. Shackleton, *Science* **289**, 1897 (2000).
19. E. A. Boyle, L. D. Keigwin, *Earth Planet. Sci. Lett.* **76**, 135 (1985).
20. M. E. Raymo, B. Grant, M. Horowitz, G. H. Rau, *Mar. Micropaleontology* **27**, 313 (1996).
21. K. T. Lawrence, T. D. Herbert, C. M. Brown, M. E. Raymo, A. M. Haywood, Paleoceanography **24**, PA2218, 10.1029/2008PA001669 (2009).
22. E. L. McClymont, A. Roselle-Mele, *Geology* **33**, 389 (2005).
23. N. J. Shackleton, *Cent. Natl. Rech. Sci. Colloq. Int.* **219**, 203 (1974).
24. R. G. Fairbanks, *Nature* **342**, 637 (1989).
25. J.-C. Duplessy, L. Labeyrie, C. Waelbroeck, *Quat. Sci. Rev.* **21**, 315 (2002).
26. M. Mudelsee, M. E. Raymo, *Paleoceanography* **20**, 10.1029/2005PA001153 (2005).
27. T. M. Cronin *et al.*, *Palaeogeogr. Palaeoclimatol. Palaeoecol.* **108**, 437 (1994).
28. A. Kitamura, T. Kawagoe, *Quat. Sci. Rev.* **25**, 323 (2006).
29. D. J. Lunt, G. L. Foster, A. M. Haywood, E. J. Stone, *Nature* **454**, 1102 (2008).
30. R. Bintanja, R. S. W. van de Wal, *Nature* **454**, 869 (2008).
31. D. A. Hodell, J. E. T. Channell, J. H. Curtis, O. E. Romero, U. Rohl, *Paleoceanography* **23**, PA4218, 10.1029/2008PA001591 (2008).
32. C. Waelbroeck *et al.*, *Quat. Sci. Rev.* **21**, 295 (2002).
33. M. Siddall *et al.*, *Nature* **423**, 853 (2003).
34. D. W. Lea, P. A. Martin, D. K. Pak, H. J. Spero, *Quat. Sci. Rev.* **21**, 283 (2002).

35. We thank J. Wright for assistance with isotope measurements and suggestions, M. Raymo for numerous discussions, and W. Zhang and K. Lawrence for assistance with time series analysis. Two anonymous reviewers provided insightful suggestions that substantially improved the manuscript. We acknowledge the ODP and Woods Hole Oceanographic Institution Seafloor Samples Laboratory for supplying sediment samples. This work was supported by a USSSP Schlanger ODP Fellowship to S.S. and NSF award OCE 02-20922 to Y.R.

Supporting Online Material

www.sciencemag.org/cgi/content/full/325/5938/306/DC1
Materials and Methods
Figs. S1 to S5
Tables S1 and S2
References

17 December 2008; accepted 10 June 2009
10.1126/science.1169938

Transient Simulation of Last Deglaciation with a New Mechanism for Bølling-Allerød Warming

Z. Liu,[1,2,3]* B. L. Otto-Bliesner,[4] F. He,[3] E. C. Brady,[4] R. Tomas,[4] P. U. Clark,[5] A. E. Carlson,[6] J. Lynch-Stieglitz,[7] W. Curry,[8] E. Brook,[5] D. Erickson,[9] R. Jacob,[10] J. Kutzbach,[3] J. Cheng[1,3]

We conducted the first synchronously coupled atmosphere-ocean general circulation model simulation from the Last Glacial Maximum to the Bølling-Allerød (BA) warming. Our model reproduces several major features of the deglacial climate evolution, suggesting a good agreement in climate sensitivity between the model and observations. In particular, our model simulates the abrupt BA warming as a transient response of the Atlantic meridional overturning circulation (AMOC) to a sudden termination of freshwater discharge to the North Atlantic before the BA. In contrast to previous mechanisms that invoke AMOC multiple equilibrium and Southern Hemisphere climate forcing, we propose that the BA transition is caused by the superposition of climatic responses to the transient CO_2 forcing, the AMOC recovery from Heinrich Event 1, and an AMOC overshoot.

The last deglaciation (~21 to 11 ka) (ka: 1000 years ago) experienced the last major natural global warming and was punctuated by several abrupt climate changes (*1*, *2*). Particularly notable changes occurred in the North Atlantic region where the surface climate experienced cooling during Heinrich Event 1 (H1, ~17 ka), followed by an abrupt warming at the onset of the Bølling-Allerød (BA, ~14.5 ka) (Fig. 1) (*2*–*11*). These abrupt climate changes were accompanied by large changes in the Atlantic meridional overturning circulation (AMOC), suggesting a causal linkage through the AMOC and its associated heat transport (*5*, *6*) (Fig. 1C).

Climate evolution during the last deglaciation has been studied in transient simulations with climate models of intermediate complexity (*12*). In particular, some intermediate models simulated abrupt warming events like the BA by triggering a resumption of the AMOC either locally by a reduced meltwater flux (MWF) (*13*) or surface warming (*14*) over the North Atlantic, or remotely by an increased MWF (*15*) or surface warming (*16*) over the Southern Ocean. In all the cases, the abrupt warming occurred in response to a gradually varying forcing (*17*) through a strong hysteresis associated with AMOC advection and North Atlantic convection (*18*). Long transient simulations, however, have not been carried out in synchronously coupled atmosphere-ocean general circulation models (CGCMs), which include the most advanced climate physics and are currently being used for future climate projections. Here we present a transient simulation of the climate evolution from the Last Glacial Maximum (LGM, ~21 ka) to BA using a state-of-art CGCM: the National Center for Atmospheric Research Community Climate System Model version 3 (NCAR CCSM3) (*19*). Through realistic changes in boundary conditions and forcing, our simulation captures many major features of the deglacial climate evolution, including the magnitude of the climate response as inferred from observations.

Starting from a previous LGM simulation (*20*), our model was integrated from 22 toward 14 ka, forced by changes in insolation (*21*), atmospheric greenhouse gas (GHG) concentrations (*22*) (Fig. 1A), continental ice sheets and coastlines (*23*, *24*), and MWF over the North Atlantic and Gulf of Mexico (Materials and Methods 1). From 22 to 19 ka, the model climate changes slowly, primarily due to insolation forcing. The simulated Atlantic Ocean at 19 ka, which we call the glacial state, captures important features of the LGM circulation as reconstructed from various proxy records (*25*, *26*), including a shallower North Atlantic Deep Water (NADW) accompanied by a southward shift of deep convection from the Nordic Seas to the Greenland Sea, a reduced AMOC transport, and a volumetric expansion of Antarctic Bottom Water (Fig. 2, A and D and figs. S1A and S2) (Materials and Methods 1).

From 19 to 17 ka, we applied a MWF derived from Northern Hemisphere ice sheets to the North Atlantic and Gulf of Mexico at a rate consistent (within uncertainties) with the record of sea-level rise (*23*, *27*), gradually reaching a peak flux of 20 m per thousand years (ky) at H1 (Fig. 1, B and C). The MWF was then reduced in two scenarios: a linear decrease to zero at 14.2 ka (DGL-B) and a constant flux (of 15 m/ky) until a sudden shut-off at 14.67 ka (DGL-A) (Materials and Methods 2). Because the meltwater termination scenarios DGL-B and DGL-A represent the slowest and fastest possible MWFs, the two corresponding experiments represent two

[1]Key Laboratory of Meteorological Disaster, Nanjing University of Information Science and Technology, Nanjing, 210044, China. [2]State Key Laboratory of Loess and Quaternary Geology, Institute of Earth Environment, Chinese Academy of Sciences, Xi'an, 710075, China. [3]Center for Climatic Research and Department of Atmospheric and Oceanic Sciences, University of Wisconsin, Madison, WI 53706, USA. [4]Climate and Global Dynamics Division, National Center for Atmospheric Research, Boulder, CO 80307–3000, USA. [5]Department of Geosciences, Oregon State University, Corvallis, OR 97331, USA. [6]Department of Geology and Geophysics and Center for Climatic Research, University of Wisconsin, Madison, WI 53706, USA. [7]School of Earth and Atmospheric Sciences, Georgia Institute of Technology, Atlanta, GA 30332, USA. [8]Geology and Geophysics, Woods Hole Oceanographic Institution, Woods Hole, MA 02543, USA. [9]Oak Ridge National Laboratory, Oak Ridge, TN 37831–6016, USA. [10]Mathematics and Computer Science Division, Argonne National Laboratory, Argonne, IL 60439–4843, USA.

*To whom correspondence should be addressed. E-mail: zliu3@wisc.edu

end members for simulations under more realistic MWF.

The increase in MWF starting at 19 ka induces a gradual decrease in the AMOC (Fig. 1D). The associated freshwater anomaly is confined initially to the upper North Atlantic at H1 (fig. S1B) and is then transported in the upper ocean into the Southern Ocean, where it eventually spreads northward in the deep ocean, substantially freshening the glacial bottom water by the time of the BA (fig. S1C). From 17 ka to the BA, the MWF decreases in both experiments, leading to increases in the AMOC. The AMOC increases gradually toward the BA following the gradual decrease in MWF in DGL-B, but it resumes abruptly at the BA following the abrupt termination of MWF in DGL-A (Fig. 1D). Regardless of the recovery speeds, however, the AMOC in both experiments peaks at ~19 sverdrup (1 sverdrup = 10^6 m^3/s) at the onset of the BA, or ~6 sverdrup greater than the glacial-state transport (~13 sverdrup), and is characterized by a deeper and stronger circulation (Fig. 2C), comparable with that in a Holocene simulation (not shown). The simulated transient responses of the AMOC from 19 to 14 ka, especially in experiment DGL-A, are in overall agreement with a reconstruction of changes in the AMOC export (Fig. 1D) (*5*).

Accompanying these changes in the AMOC is a bipolar seesaw response in surface temperature until H1, followed by a global warming that peaks at the BA. The bipolar seesaw response is characterized by a cooling over the Northern Hemisphere and a warming over the Southern Hemisphere (Fig. 3A) and is caused by a decrease in the northward heat transport of the AMOC (*28*–*30*). The suppression of convection also contributes to the strong surface cooling in the North Atlantic. A weak warming also occurs over North America and northern Europe due to the lowering of the ice sheets and the associated response of the planetary waves (*31*). By contrast, the warming from H1 to BA is global, with the maximum warming relative to H1 exceeding 20°C in the North Atlantic and Arctic (Fig. 3B). A large fraction of this BA warming, or that part relative to the glacial state (Fig. 3C), is characterized by a polar amplification in both hemispheres.

The simulated global temperature evolution closely resembles paleoclimate reconstructions [supporting online material (SOM) Text 1], although there is a tendency for a model-data discrepancy before 19 ka, which may be attributed partly to our initial state of an equilibrium climate at LGM. Focusing on the Atlantic sector here, the simulated annual temperature closely follows the trajectory of temperature reconstructions from Greenland (Fig. 1E) and Antarctic (Fig. 1F) ice cores. From 21 to 19 ka, both Greenland and Antarctica show a weak early warming of ~0.5°C, which we attribute to increased obliquity and associated sea-ice feedback (*32*, *33*). With the increased MWF from 19 to 17 ka, temperature decreases by 4°C over Greenland but increases by 2°C over Antarctica, reflecting the bipolar seesaw response (Fig. 3A). The most pronounced changes occur in response to the decrease in MWF from 17 to 14 ka. Simulated Greenland temperature increases by 15°C at the BA onset, comparable with temperature reconstructions (*7*, *34*). By contrast, Antarctic temperature continues to increase toward the BA, as in ice-core reconstructions (*35*), which is caused primarily by the rapid increase in GHG concentrations during this period (SOM Text 2).

The characteristic North Atlantic temporal evolutionary structure of H1 cooling followed by BA warming simulated by CCSM3 is also in good agreement with sea-surface temperature (SST) reconstructions from the eastern subtropical gyre off the Iberian Margin (Fig. 1G). Over the tropical Atlantic, model SSTs first decrease toward H1 and then recover sharply at the BA, accompanied by a suppression of rainfall toward the H1 and a subsequent recovery toward the BA. The simulated rainfall suppression toward H1 (enhancement at BA) is caused by the southward (northward) migration of the Intertropical Convergence Zone (ITCZ), which is induced by the surface ocean warming south (north) of the equator in response to the increased (decreased) freshwater forcing (*36*). The simulated abrupt increase of SSTs and rainfall at the onset of the BA, especially in experiment DGL-A, generally

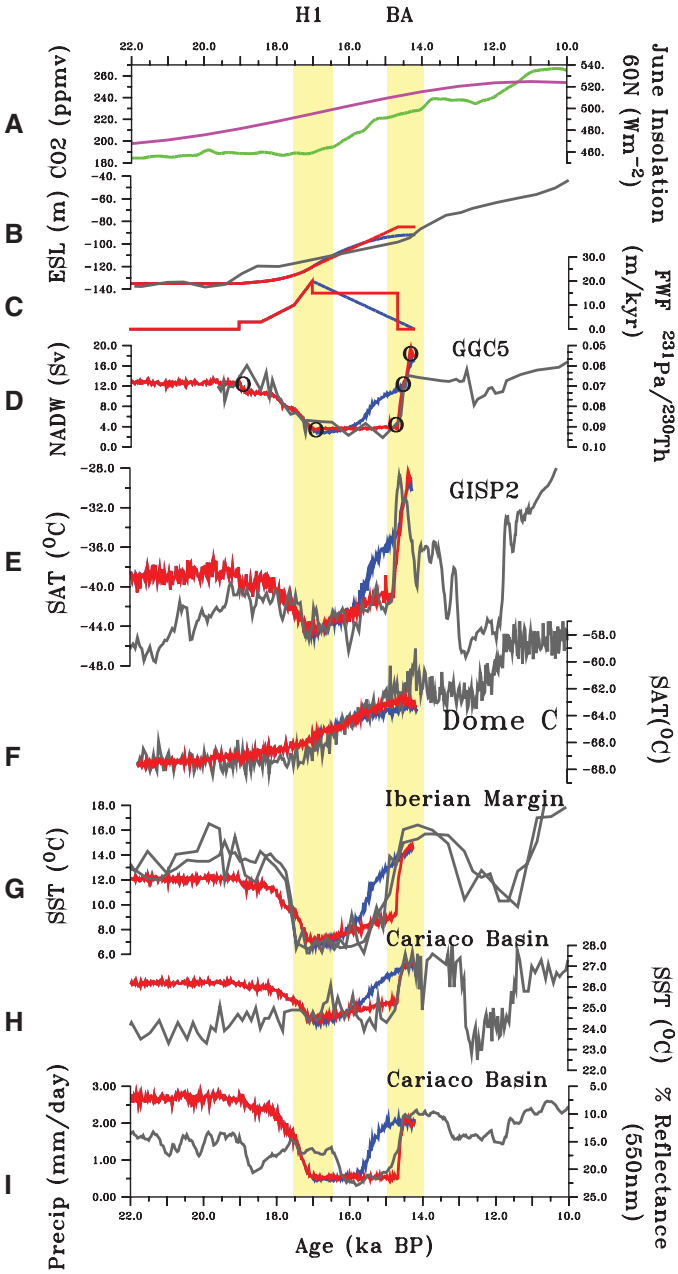

Fig. 1. Data-model comparison for several benchmark time series. (**A**) June insolation at 60°N (purple) (*21*) and atmospheric CO_2 concentration (green) (*22*). ppmv, parts per million by volume. (**B**) Sea level from the reconstruction (gray) (*23*) and model [meters of equivalent global sea level (ESL) for meltwater]. (**C**) Freshwater fluxes (FWF) in the model. (**D**) Pa/Th ratio at Bermuda (GGC5 core) as a proxy for AMOC export (*5*), and model maximum AMOC transport (below 500 m). (**E**) Greenland surface air temperature (SAT) based on Greenland Ice Sheet Project 2 (GISP2) $\delta^{18}O$ reconstruction with borehole temperature calibration (*34*) and in the model (model offset by –3°C). (**F**) Antarctic surface air temperature based on Dome C $\delta^{18}O$ reconstruction (*35*) and in the model. (**G**) SST from the Iberian Margin from reconstructions (*8*, *9*) and model. (**H**) SST from the Cariaco Basin from reconstruction (*10*) and model (model offset by 4°C). (**I**) Rainfall in Cariaco Basin from reconstruction (*11*) and model. In (B) to (I), gray is used for the reconstruction, and red and blue for experiments DGL-A and DGL-B, respectively. The five circles on DGL-A in (D) represent the glacial state (GLA, 19 ka), H1 (17 ka), PreBA (14.7 ka), Recovery (REC, 14.5 ka), and BA (14.35 ka). All model variables are annual means with a 20-year running average. Overall, model simulations, especially DGL-A, are in good agreement with the proxy records, especially outside the tropical Atlantic. BP, before present.

agree with the Cariaco Basin reconstructions (Fig. 1, H and I), although the simulated earlier decrease in the SST and rainfall toward H1 seems to be largely absent in the reconstructions. Overall, the model overestimates the climate variability associated with the ITCZ over the tropical Atlantic. This overestimation is likely caused by a double ITCZ bias in the model tropical Atlantic climatology—a common deficiency in most current CGCMs (*37*).

In contrast to the bipolar seesaw temperature response at the ocean surface, the subsurface ocean warms throughout the Atlantic during the MWF period from H1 to the BA (Fig. 2, E and F), providing a heat reservoir potentially important for the subsequent BA warming. The subsurface warming is largely consistent with previous experiments and observations (*38*). In the North Atlantic, the surface freshening suppresses the convective heat exchange, cooling the surface but warming the subsurface. The subsequent reduction of the AMOC and associated northward heat transport warms the entire South Atlantic water column, but further cools the surface North Atlantic.

Previous studies of the BA in simplified models found that the abrupt warming was caused by a sudden resumption of the AMOC in response to a gradual perturbation forcing, reflecting a strongly nonlinear response to MWF associated with substantial AMOC hysteresis (*13*–*16*). By contrast, CCSM3 simulates the BA warming largely as a linear response to MWF, with most of the abrupt warming occurring only in response to a sudden termination of the MWF. Indeed, CCSM3 has no appreciable hysteresis (SOM Text 3). This is best illustrated in experiment DGL-B from 19 to 14 ka (*39*, *40*), whereby the AMOC decreases gradually from 19 to 17 ka when the MWF increases gradually, but then recovers gradually from 17 to 14.2 ka when the MWF decreases slowly, eventually overshooting beyond the glacial transport (Fig. 1, C and D) (*41*).

Both experiments DGL-A and DGL-B simulate a ~15°C warming over Greenland from H1 to BA, comparable with temperature reconstructions (*7*, *34*) (Fig. 1). Of this amount, 5°C is associated with the AMOC recovery from H1 back to the glacial state, and the remaining 10°C results from the CO_2-induced warming and an AMOC overshoot (the AMOC recovery beyond the glacial-state transport). The approximate contributions of the three mechanisms can be assessed from experiment DGL-A. First, the total radiative warming due to CO_2 and orbital forcing in the absence of AMOC change can be estimated as the difference between the pre-BA (14.67 ka) and H1 states. In this period, the MWF and, in turn, the collapsed AMOC remain unchanged in DGL-A (Fig. 1, C and D), so that the warming is caused primarily by the radiative forcing. Indeed, from H1 to pre-BA, both Greenland and Antarctica exhibit a similar gradual warming of ~4°C (Fig. 1, E and F). This symmetric warming (fig. S6A) is consistent with the symmetric radiative forcing of CO_2 and annual insolation. Our further sensitivity experiments show, however, that this warming is dominated by the CO_2 forcing, whereas the contribution of the orbital forcing is weak (SOM Text 2). Indeed, the period from 17 to 14.6 ka saw the first major rise of the GHGs, with a 40-ppm (parts per million) increase in CO_2 accounting for about half of the glacial-interglacial change (Fig. 1A). This large increase in CO_2 induces a symmetric global warming background for the subsequent BA warming.

Upon the suspension of the MWF after 14.67 ka in experiment DGL-A, the AMOC recovers rapidly to its glacial level by ~14.5 ka, with a 5°C warming over Greenland (Fig. 1, D and E). This recovery warming is of the same magnitude as the H1 cooling, reflecting a nearly linear dependence of Greenland temperature on AMOC strength. In contrast to the bipolar response to the MWF during H1 (Fig. 3A), however, the rapid warming due to AMOC recovery is confined to the North Atlantic and Arctic regions (Fig. 1, E to H, and fig. S6B).

Finally, after the recovery at 14.5 ka, Greenland temperature increases by another 6°C, peaking at 14.35 ka (Fig. 1E), accompanied by an AMOC overshoot beyond its glacial level by ~6 sverdrup (Fig. 1D). This BA overshoot, which generates a strong warming over the Nordic Sea region (Fig. 1, E to H, and fig. S6C), is caused by a natural overshoot of the AMOC at the end of MWF, which is further enhanced by the long duration of the MWF and the large CO_2 rise from H1 to the BA. The overshoot appears to be caused by convective instability in the Nordic Sea on a background of deep-ocean warming (Fig. 2, E and F), as well as a basin-wide advective adjustment of salinity (SOM Text 4).

In contrast to the robust warming magnitude, the warming rate of the BA in CCSM3 depends critically on the MWF scenario. A faster reduction in MWF induces a more rapid BA warming, as seen by comparing experiments DGL-A and DGL-B. The sudden termination of MWF in DGL-A produces an abrupt BA warming that strongly resembles proxy records (Fig. 1), although the model warming is somewhat slower than in these records (300 versus 150 years, fig. S4). Because the natural adjustment time of the AMOC is ~300 years (as seen in experiment DGL-A), a similar abrupt BA warming can be induced in this model as long as there exists a substantial reduction of MWF several centuries before the Bølling onset. Because the two MWF scenarios DGL-A and DGL-B represent the end members, a more realistic MWF scenario that lies in between may also induce a rather rapid BA warming in CCSM3 (*42*). We conclude that the critical factor for producing the abruptness of the BA warming in CCSM3 is that the MWF to the North Atlantic keeps the AMOC near its off-state to within centuries of the Bølling onset, while other details of the meltwater history may not be essential.

We find that CCSM3 is able to simulate an abrupt BA warming as a transient response to a

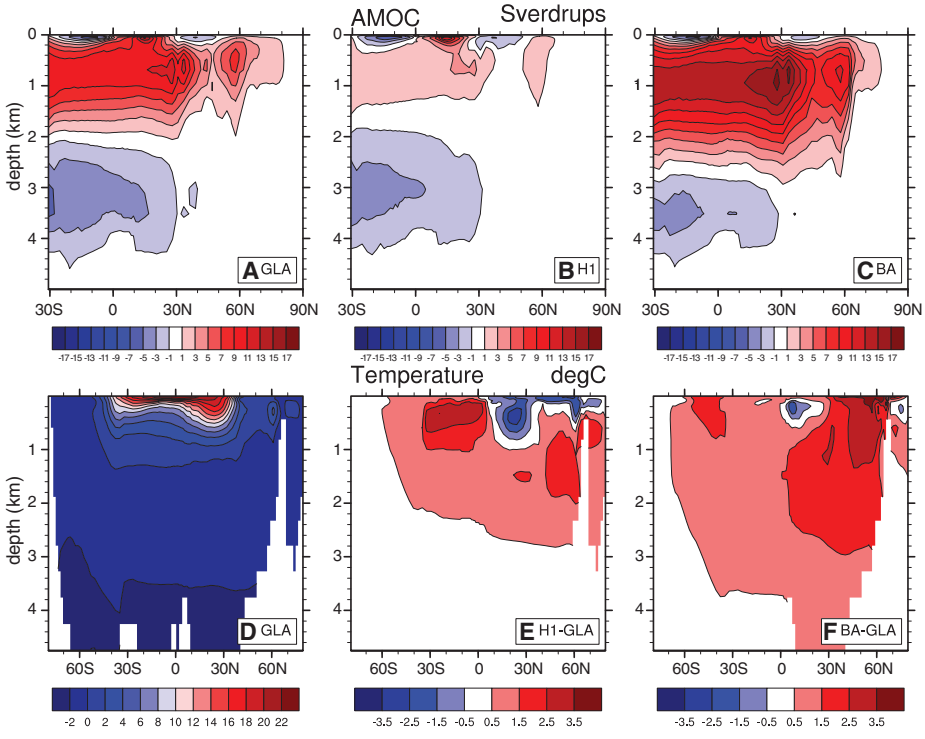

Fig. 2. AMOC streamfunction (in sverdrup) and Atlantic zonal mean temperature and temperature changes in experiment DGL-B (in °C). AMOC at (**A**) GLA, (**B**) H1, and (**C**) BA. Temperature at (**D**) GLA and temperature changes from the glacial state for (**E**) H1-GLA and (**F**) BA-GLA. The AMOC collapses in H1 and overshoots beyond the glacial state at BA. The subsurface ocean warms throughout the Atlantic, whereas the SST exhibits a bipolar seesaw response. (Each state is defined in Fig. 1D).

sudden termination of the North Atlantic MWF. The amplitude of the simulated BA is comparable to the amplitude reconstructed from paleoclimate proxies, notably in the North Atlantic and Antarctic regions. Our simulation suggests that the large BA warming is caused by the superposition of climate responses to increased atmospheric CO_2, the recovery of the AMOC from H1, and an AMOC overshoot. It remains uncertain if CCSM3 is successful in simulating the abruptness of the BA warming inferred in proxy records. CCSM3 can produce the abruptness of the BA onset only if the MWF in the North Atlantic terminates within centuries before the BA. This is in contrast to previous work in simplified models, which exhibit a substantial AMOC hysteresis (*39*) such that an abrupt warming can be induced by a gradual change in MWF. The behavior of CCSM3, however, is typical of the current generation of CGCMs without flux adjustment, which show little sign of substantial hysteresis (*30*, *43*). Therefore, our results suggest that the current generation of CGCMs, like CCSM3, may not be able to induce an abrupt onset of BA warming under a gradual forcing. Is the current generation of CGCMs deficient in generating the abruptness of climate changes (*44*)? Is the AMOC hysteresis a fundamental feature of the real-world AMOC as suggested in intermediate models, or not essential as suggested in current CGCMs? Current observations are insufficient to address these questions unambiguously (SOM Text 5). We suggest that the critical observational evidence needed to clarify these fundamental issues is an accurate reconstruction of the rate of MWF before the BA.

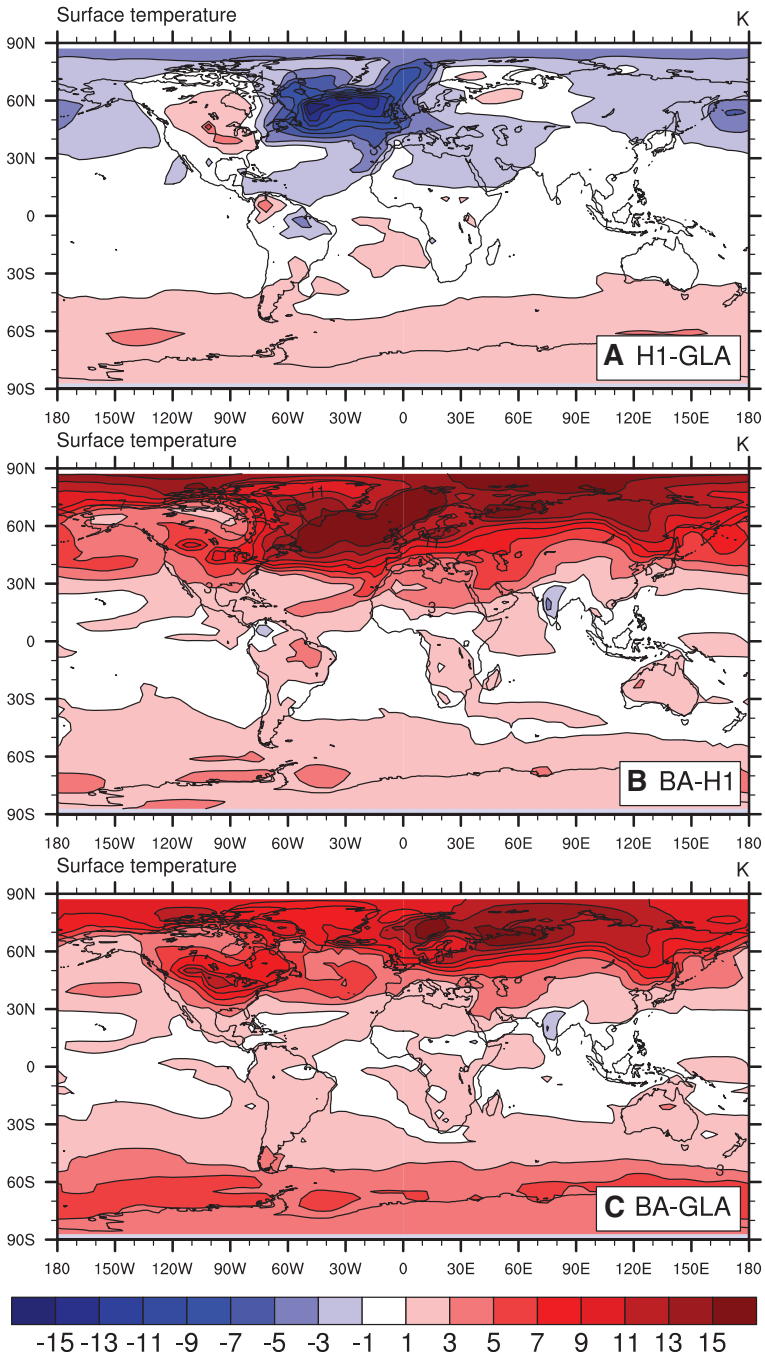

Fig. 3. Surface air temperature changes (in °C) in experiment DGL-B. (**A**) H1 temperature anomaly from the glacial state, (**B**) BA temperature anomaly from H1, and (**C**) BA temperature anomaly from GLA. The H1 temperature response exhibits a bipolar seesaw; the BA warming is dominated by a maximum warming at northern high latitude (B) over H1, but exhibits a more symmetric warming (C) over the glacial state. (Each state is defined in Fig. 1D.)

References and Notes

1. W. S. Broecker, *Paleoceanography* **13**, 119 (1998).
2. P. U. Clark, N. G. Pisias, T. F. Stocker, A. J. Weaver, *Nature* **415**, 863 (2002).
3. P. M. Grootes *et al.*, *Nature* **366**, 552 (1993).
4. R. B. Alley, P. U. Clark, *Annu. Rev. Earth Planet. Sci.* **27**, 149 (1999).
5. J. F. McManus, R. Francois, J.-M. Gherardi, L. Keigwin, S. Brown-Leger, *Nature* **428**, 834 (2004).
6. E. Boyle, L. Keigwin, *Nature* **330**, 35 (1987).
7. J. P. Severinghaus, E. J. Brook, *Science* **286**, 930 (1999).
8. C. Waelbroeck *et al.*, *Paleoceanography* **13**, 272 (1998).
9. E. Bard, F. Rostek, J.-L. Turon, S. Gandreau, *Science* **289**, 1321 (2000).
10. D. W. Lea, D. K. Pak, L. C. Peterson, K. A. Hughen, *Science* **301**, 1361 (2003).
11. L. C. Peterson, G. H. Haug, K. A. Hughen, U. Rohl, *Science* **290**, 1947 (2000).
12. In these simplified models, however, the transient simulations have not been carried out in a synchronously coupled mode under the complete climate forcing (notably the meltwater forcing), (*45*, *46*).
13. A. Ganopolski, S. Rahmstorf, *Nature* **409**, 153 (2001).
14. G. Knorr, G. Lohmann, *Geochem. Geophys. Geosyst.* **8**, Q12006 (2007).
15. A. J. Weaver, O. A. Saenko, P. U. Clark, J. X. Mitrovica, *Science* **299**, 1709 (2003).
16. G. Knorr, G. Lohmann, *Nature* **424**, 532 (2003).
17. The nature of the AMOC resumption is complex from the perspective of a dynamic system (*47*) and is beyond the scope of this study.
18. S. Rahmstorf, *Nature* **378**, 145 (1995).
19. S. G. Yeager, C. A. Shields, W. G. Large, J. J. Hack, *J. Clim.* **19**, 2545 (2006).
20. B. L. Otto-Bliesner *et al.*, *J. Clim.* **19**, 2526 (2006).
21. A. Berger, *J. Atmos. Sci.* **35**, 2362 (1978).
22. F. Joos, R. Spahni, *Proc. Natl. Acad. Sci. U.S.A.* **105**, 1425 (2008).
23. W. R. Peltier, *Annu. Rev. Earth Planet. Sci.* **32**, 111 (2004).
24. For technical reasons, river run-off routing is kept as at the present.
25. B. L. Otto-Bliesner *et al.*, *Geophys. Res. Lett.* **34**, L12706 (2007).
26. J. Lynch-Stieglitz *et al.*, *Science* **316**, 66 (2007).
27. P. U. Clark, A. C. Mix, *Quat. Sci. Rev.* **21**, 1 (2002).
28. T. Crowley, *Paleoceanography* **7**, 489 (1992).
29. T. F. Stocker, *Science* **282**, 61 (1998).
30. R. Stouffer *et al.*, *J. Clim.* **19**, 1365 (2006).
31. S. W. Hostetler, P. U. Clark, P. J. Bartlein, A. C. Mix, N. G. Pisias, *J. Geophys. Res.* **104**, 3947 (1999).
32. S.-I. Shin, Z. Liu, B. Otto-Bliesner, J. Kutzbach, S. J. Vavrus, *Geophys. Res. Lett.* **30**, 1096 (2003).
33. A. Timmermann, O. Timm, L. Stott, L. Menviel, *J. Clim.* **22**, 1626 (2009).
34. K. Cuffey, G. Clow, *J. Geophys. Res.* **102**, 26383 (1997).
35. J. Jouzel *et al.*, *Science* **317**, 793 (2007).
36. R. Zhang, T. Delworth, *J. Clim.* **18**, 1853 (2005).
37. M. K. Davey *et al.*, *Clim. Dyn.* **18**, 403 (2002).

38. This subsurface warming is qualitatively similar to that of previous experiments with North Atlantic MWF, especially in the tropical region and Southern Hemisphere [e.g., (*30*, *48*)]; it seems also to be consistent with benthic $\delta^{18}O$ inferred temperature changes in the tropical Atlantic (*49*), western subtropical North Atlantic (*4*), and Nordic Sea (*50*), as well as Mg/Ca-based benthic temperatures from the eastern subtropical North Atlantic (*51*).
39. S. Rahmstorf *et al.*, *Geophys. Res. Lett.* **32**, L23605 (2005).
40. The MWF varies slowly during this period at a rate of ~0.1 sverdrup/ky in DGL-B, comparable to that used in previous standard hysteresis tests (*18*, *39*).
41. About a third of the model BA warming appears to be associated with a nonlinear convective response in the Nordic Sea. As seen in experiment DGL-B, under a gradual forcing, the AMOC and Greenland temperature, after a long period of gradual change, increase abruptly at the end stage (14.6 ka) in 100 years (6 sverdrup and 6°C), nearly identical to the last 100 years of warming in experiment DGL-A (Fig. 1, D and E, and fig. S4). This abrupt warming is induced by regional convective instability in the Nordic Sea (*18*) on a background deep-ocean warming (*52*) and is enhanced by the northward heat transport associated with the enhanced AMOC.
42. With a slower reduction in MWF, the AMOC resumption and attendant BA warming in CCSM3 usually occur faster than the rate at which the MWF is reduced, partly due to the convective instability process in the Nordic Sea (*41*). In a deglaciation sensitivity experiment similar to DGL-B, but with a faster termination time of 2000 years, the BA warming takes only 500 years, substantially faster than the MWF itself (not shown).
43. Except for an earlier generation of CGCM with flux adjustments (*53*, *54*), all published results from CGCMs are similar to those of CCSM3 in showing that the AMOC recovers its strength after the termination of the freshwater pulse. Because these CGCM hosing experiments are usually short (<1000 years), they are not strict tests for the hysteresis of AMOC (*18*). Nevertheless, these models have shown little sign of substantial hysteresis.
44. A diagnosis of nine coupled climate models, including both CGCMs and intermediate models, suggests a positive bias in the freshwater transport by the AMOC in the South Atlantic, which may imply a bias toward a more stable AMOC and therefore a lack of multiple equilibria and in turn substantial hysteresis in these climate models (*55*). Further study is needed, however, to understand the stability of the AMOC in coupled climate models, especially in state-of-art CGCMs.
45. D. J. Lunt, M. S. Williamson, P. J. Valdes, T. M. Lenton, *Clim. Past Discuss.* **2**, 267 (2006).
46. O. Timm, A. Timmermann, *J. Clim.* **20**, 4377 (2007).
47. J. Abshagen, A. Timmermann, *J. Phys. Oceanogr.* **34**, 2756 (2004).
48. S. Manabe, R. Stouffer, *Paleoceanography* **12**, 321 (1997).
49. C. Ruhlemann *et al.*, *Paleoceanography* **19**, PA1025 (2004).
50. T. L. Rasmussen, E. Thomsen, *Palaeogeogr. Palaeoclimatol. Palaeoecol.* **210**, 101 (2004).
51. L. Skinner, N. Shackleton, *Quat. Sci. Rev.* **25**, 3312 (2006).
52. J. Mignot, A. Ganopolski, A. Levermann, *J. Clim.* **20**, 4884 (2007).
53. S. Manabe, R. Stouffer, *J. Clim.* **1**, 841 (1988).
54. J. Yin, R. Stouffer, *J. Clim.* **20**, 4293 (2007).
55. S. Weber *et al.*, *Clim. Past Discuss.* **3**, 51 (2007).
56. We thank A. Ganoposki, J. Marotzke, and A. Timmermann for helpful discussions and two reviewers for comments. This research was supported mainly by the Paleoclimate Program of NSF, NCAR, and Chinese NSF (NSFC40875058). The computing is supported by the U.S. Department of Energy INCITE program and Abrupt Climate Change Program. This paper is CCR contribution No. 980.

Supporting Online Material

www.sciencemag.org/cgi/content/full/325/5938/310/DC1
Materials and Methods
SOM Text
Figs. S1 to S7
References and Notes
Movie S1

16 January 2009; accepted 2 June 2009
10.1126/science.1171041

Undulatory Swimming in Sand: Subsurface Locomotion of the Sandfish Lizard

Ryan D. Maladen,[1] Yang Ding,[2] Chen Li,[2] Daniel I. Goldman[1,2]*

The desert-dwelling sandfish (*Scincus scincus*) moves within dry sand, a material that displays solid and fluidlike behavior. High-speed x-ray imaging shows that below the surface, the lizard no longer uses limbs for propulsion but generates thrust to overcome drag by propagating an undulatory traveling wave down the body. Although viscous hydrodynamics can predict swimming speed in fluids such as water, an equivalent theory for granular drag is not available. To predict sandfish swimming speed, we developed an empirical model by measuring granular drag force on a small cylinder oriented at different angles relative to the displacement direction and summing these forces over the animal movement profile. The agreement between model and experiment implies that the noninertial swimming occurs in a frictional fluid.

The locomotion of organisms (*1*, *2*), whether by running, flying, swimming, or crawling, is the result of multiple-degree-of-freedom nervous and musculoskeletal systems interacting with an environment that often flows and deforms in response to movement. Nearly all experiments and models of terrestrial locomotion have been developed for running and walking on rigid, flat, no-slip frictional substrates for which the complication of substrate flow is not considered. In contrast, complexity in interaction with the environment in aquatic and aerial locomotion (swimming and flying) is well recognized (*3*). Determining mechanisms for propulsion or lift in these media is always possible in principle because the rules of interaction with fluids are worked out: They require solving Navier-Stokes hydrodynamics in the presence of moving boundary conditions. A major challenge in biology is to understand the locomotion of organisms that walk, crawl, or burrow on or within terrestrial substrates like sand (*4*), soil (*5*), and muddy sediments (*6*) that display both solid and fluidlike behavior. In such materials, validated theories such as the Navier-Stokes equations for fluids do not exist, and visualization techniques [such as particle image velocimetry in fluids (*7*)] are nearly nonexistent. Understanding of the mechanics of subsurface movement has ecological importance and could reveal how the actions of small burrowing organisms can transform entire landscapes (*8*).

Animal burrowing and movement within granular media is relevant to desert organisms like scorpions, snakes, and lizards that move within sand to escape heat and predators and hunt for prey (*9*, *10*). Desert sand [which covers 6 to 10% of land surface (*11*)] is an example of a granular material, a collection of dissipative particles that interact through contact forces and in bulk can display solid and fluidlike features (*12*) when disturbed. A key parameter that controls the response of granular media to intrusion is the volume fraction ϕ, the ratio of material volume to total occupied volume. In dry granular media in natural environments, ϕ depends on the history of the sand (for example, perturbations by wind or animal burying and digging), and can vary between 0.57 and 0.64 (*13*). The response of granular media to intrusion depends on ϕ: Closely packed material at high ϕ must expand to flow, whereas loosely packed material at low ϕ consolidates (*14*). The effects of ϕ on drag are largely unexplored, although we have recently found that vertical penetration resistance doubles as ϕ increases by just 0.08 (*15*).

To investigate how rheological features of the material influence the locomotor mode and performance of an organism moving within sand, we used high-speed x-ray imaging to study a small (~10 cm) desert-dwelling lizard, the sandfish, that inhabits the Saharan desert of Africa and moves within granular media of different ϕ. The sandfish's above-ground burial process has been described (*9*), and it is hypothesized that its counter-sunk lower jaw and smooth scales with low friction and low wear properties (*16*) aid swimming and digging. However, little is known about how the animal moves subsurface. Although it has been hypothesized that body motion plays an important role in thrust production (*9*, *17*) in sand-dwelling lizards, a recent study using nuclear magnetic resonance (NMR) to visualize subsurface motion proposed that the sandfish used its limbs in a paddling motion along with undulations on its body to generate thrust subsurface (*18*). However, the observa-

[1]Interdisciplinary Bioengineering Program, Georgia Institute of Technology, Atlanta, GA 30332, USA. [2]School of Physics, Georgia Institute of Technology, Atlanta, GA 30332, USA.

*To whom correspondence should be addressed. E-mail: daniel.goldman@physics.gatech.edu